



Reflector Deformation Measurement and Correction Methodology of Large Antenna Based on Phased Array Feed

Zan Wang^{1,2}, De-Qing Kong^{1,2,4}, Hong-Bo Zhang^{1,2,4}, Yan Su^{1,2}, Xin-Ying Zhu^{1,2}, Cong-Si Wang³, and Yu-Chen Liu^{1,2} 
¹ Key Laboratory of Lunar and Deep Space Exploration, National Astronomical Observatories, Chinese Academy of Sciences, Beijing 100101, China; kdq@bao.ac.cn, zhanghb@nao.cas.cn

² University of Chinese Academy of Sciences, Beijing 100049, China

³ Key Laboratory of Electronic Equipment Structure Design, Ministry of Education, Xidian University, Xi'an 710071, China
Received 2023 December 29; revised 2024 January 29; accepted 2024 February 8; published 2024 March 19

Abstract

To solve the problem of time-consuming measurement and correction of large antennas' reflector deformation, a new microwave holography methodology based on a Phased Array Feed (PAF) is proposed. Starting from the known expression of receiving signals in microwave holography, the theory of PAF holography is derived through Geometrical Optics. Reflector deformation, as well as pointing deviation and subreflector offset, can be calculated out by applying the derived equations. A measurement and correction system based on PAF holography is depicted, and two kinds of measurement methods are illustrated. The proposed measurement methodology is verified by numerical simulation, and its measurement error is analyzed. The results indicate that our proposed methodology is feasible, especially for Cassegrain antennas.

Key words: telescopes – methods: analytical – methods: numerical

1. Introduction

Large reflector antennas are very important tools for deep space exploration and radio astronomy research. To ensure that they are working effectively, it is necessary to regularly measure the reflector surface accuracy, and correct the reflector deformation in time. As reflector antennas' aperture diameter and working frequency continue to increase, their performance is increasingly affected by their own gravity, wind load from the environment, and Sun irradiation, making it much more difficult to measure and correct the reflector deformation. As a result, how to control reflector antenna's deformation during the increase in aperture diameter and working frequency, has become a very important and popular research topic.

Large single aperture antennas all over the world mainly include Sardinia 64 m Radio Telescope (SRT; Carretti et al. 2017), Tianma 65 m Telescope (Dong & Liu 2021), Jiamusi 66 m Radio Telescope (Yu et al. 2016), Wuqing 70 m Radio Telescope (WRT; Guo et al. 2021), Deep Space Station 14 (DSS-14) 70 m Radio Telescope (Imbriale & Hoppe 2000), Lovell 76 m Telescope (Morison 2007), Effelsberg 100 m Radio Telescope (Holst et al. 2014), Green Bank 100 m Telescope (GBT; Roshi et al. 2018), Arecibo 305 m Radio Telescope (ruined, under reconstruction) (Burnett et al. 2020), Five-hundred-meter Aperture Spherical radio Telescope (FAST; Tang 2015), and QiTai 110 m Radio Telescope (QTT, under construction) (Wang 2014), etc. To measure the reflector surface

accuracy of these large radio telescopes, primary measurement methodologies including photogrammetry (Gale et al. 2016), laser scanning (Holst et al. 2017), and microwave holography (Serra et al. 2012) are developed and successfully applied. Among these measurement methods, microwave holography is widely used (Rochblatt 1998; Hunter et al. 2011; Serra et al. 2012; Liu et al. 2016; Wang et al. 2017, 2019, 2022) due to its advantages of low cost, high precision, and short measurement time. Its improvement method has reduced the measurement time to 8 minutes (Dong & Liu 2021). Once the reflector deformation is obtained, the adjustment value at each point on the reflector surface can be calculated. Then, we can correct the reflector deformation manually or by actuators mounted on antennas' back frame or using a deformable plate (Wang et al. 2013). It can be found that these correction methods are essentially considered from mechanical adjustment. However, in practice, the mechanical adjustment methods can no longer be feasible for large reflector antennas under certain working conditions. For example, when the WRT operates at the X band in fresh gale weather, i.e., force 8 wind, its signal-to-noise ratio (S/N) would decrease by more than 6 dB and fluctuates violently. Obviously, mechanical adjustment cannot keep up with the changing speed of wind load. We have also measured the antenna G/T value, i.e., ratio of gain to noise temperature, at the X band in daylight and found that it dropped by over 1.5 dB because of Sun irradiation. As for higher working frequency, e.g., at the Ka band, the G/T value would drop by over 15 dB, and the antenna efficiency would be very low. In summary, all these traditional

⁴ Corresponding authors.



(a) Parkes PAF
Chippendale et al. 2016



(b) GBT PAF
Roshi et al. 2018



(c) WSRT PAF
Van Cappellen et al. 2022

Figure 1. PAFs that have been successfully applied to large reflector antennas.

measurement and correction methods are difficult to achieve real-time measurement and correction of antenna deformation caused by wind and Sun irradiation. Therefore, we need to consider electrical adjustment, which is using a Phased Array Feed (PAF) for reflector deformation compensation.

One significant benefit that electrical adjustment has on reflector surface deformation correction is its fast response. By electronically changing the amplitude and phase excitation of each feed element of the PAF, we will be able to accomplish deformation correction indirectly and instantaneously (Wang et al. 2013; Wu 2013). Rudge & Davies (1970) is probably the first research paper which analytically and quantitatively studied using linear array feeds to instantaneously correct cylindrical reflectors having one-dimensional distortion profiles. Instead of using linear array feeds, Amitay & Zucker (1972) analyzed the use of planar array feeds for compensating spherical reflector aberrations. However, in this case, the compensation procedure relies heavily on the circular symmetry of the feed-plane field distribution. Blank & Imbriale (1988) proposed an algorithmic procedure for the synthesis of planar array feeds for paraboloidal reflectors to provide simultaneously electronic correction of systematic reflector surface distortions as well as a vernier electronic beamsteering capability. The numerical result shows that with a one ring (seven-element) array feed, 0.7 dB on-axis gain can be recovered of a 1 dB distortion loss with an optimal single feed. Rahmat-Samii (1990) carried out an experimental study using a 16-element array feed and a 19-element array feed to perform electrical compensation. The measured antenna patterns indicate that the antenna's overall gain is improved and sidelobe level is reduced after compensation. These literatures have given us a clear idea of how to use a properly excited array feed to correct the distorted antenna pattern caused by different known reflector deformations, e.g., periodic and random surface distortions (Rudge & Davies 1970), slow-varying surface distortions (Rahmat-Samii 1990). However, none of them has given a formula for calculating an antenna's reflector deformation based on its focal field. This paper will

deduce that formula in Section 2.1. Besides, their deformation correction methodologies are limited to electrical compensation, focusing on developing various array feed exciting methods to achieve higher on-axis gain or better beamsteering capability. This limits the further improvement of antenna performance because of the remained mechanical deformation. It is reasonable to combine electrical compensation and mechanical adjustment methods to further improve an antenna's overall performance by establishing a feedback network, in which the feedback information, i.e., the current reflector deformation, is provided by an array feed. This idea will be illustrated in more detail in Section 2.3.

As so far, the PAF technology is mainly used for neutral hydrogen intensity survey (Li et al. 2021), pulsar observation (Deng et al. 2017), and space debris monitoring at Low Earth Orbit (LEO; Schirru et al. 2019), etc. Chippendale et al. (2016) has successfully deployed a PAF, as shown in Figure 1(a), on the Parkes 64 m radio telescope and later on the Effelsberg 100 m telescope. The aperture efficiency of the Parkes 64 m radio telescope with PAF mounted at the focus ranges from 70% to 80%, which is very high. The working frequency of Mk. II ASKAP PAF ranges from 0.8 to 1.74 GHz, and it has made some achievements in neutral hydrogen intensity survey and pulsar observation (Deng et al. 2017; Li et al. 2021). The National Radio Astronomy Observatory (NRAO), the Green Bank Observatory (GBO), and Brigham Young University (BYU) have cooperated to design and produce a PAF for GBT. It contains 19 bipolar dipoles, as shown in Figure 1(b). The PAF works at 1.4 GHz, and increases the speed of sky survey by 2.1 to 7 times (Roshi et al. 2018). Besides, large reflector antennas including Australian Square Kilometer Array Pathfinders (ASKAP), Arecibo 305 m Radio Telescope, the Westerbork Synthesis Radio Telescope (WSRT), SRT, FAST, and QTT, are already or planned to be equipped with PAF (Han & Zhong 2016; Beresford et al. 2017; Navarrini et al. 2019; Burnett et al. 2020; Pei et al. 2022; Van Cappellen et al. 2022).

Most PAFs mentioned above work at the L band, which is a relatively low working frequency. When antennas work at low

Table 1
Antenna Deformation and their Influencing Factors, Characteristics

Influencing Factors	Antenna Deformation	Characteristics
Gravity	Pointing deviation Main reflector deformation Feed/subreflector offset	Predictable; Slowly changing; Easy to measure and correct
Wind load	Pointing deviation Servo tracking system error Main reflector deformation Feed/subreflector offset	Rapidly changing; Hard to measure and correct
Sun irradiation	Pointing deviation Main reflector deformation Feed/subreflector offset	Slowly changing; Hard to measure and correct

working frequencies, according to Ruze (Ruze 1966), the actual impact of reflector deformation on antenna performance is relatively small, so electrical compensation is not needed. When the working frequency increases, electrical compensation will become essential. However, the production of a PAF working at high frequencies is difficult. It is partly due to the significant mutual coupling effect of tightly packed feed elements at high frequencies (Wu et al. 2013). Furthermore, considering that the main lobe of antennas working at high frequencies is very narrow, and according to the reciprocity principle (Balanis 2005), slight deformation of antennas' pitch and azimuth motion supporting mechanism can cause the receiving signal convergence point to drift out of the receiving range, so using electrical compensation alone cannot meet the measurement and correction requirements. From this point of view, it is also reasonable that mechanical adjustment and electrical compensation methods should be combined and used for different types and sizes of antenna deformations to achieve the best overall performance. Here, we classify the antenna deformations into several kinds in Table 1. According to different structures, the deformations can mainly be divided into pointing deviation, servo tracking system error, main reflector deformation, and feed offset for single reflector antennas or subreflector offset for Cassegrain antennas. The deformations can also be divided into large and small deformation, or slowly changing predictable deformation and rapidly changing deformation. For example, the deformation caused by antennas' gravity is usually related to the elevation angle. It is slowly changing and predictable. However, the deformation caused by wind load is generally changing rapidly and hard to measure and correct.

Through focal field analysis, we will be able to obtain and identify the deformation information from different antenna structures. The deformation information then can be fed back to the pitch and azimuth drive system, main reflector surface control system, subreflector control system, and electrical compensation system, to ensure that the antenna always

operates in its optimal state. The measurement and correction methodology based on PAF is detailed in Section 2. In Section 3, the focal field of Wuqing 70 m Radio Telescope is simulated based on the reflector surface profile data obtained from laser scanning and empirical equations, and by applying the PAF holography equations, the distorted reflector surface is recovered. The measurement error is also analyzed in this section.

2. PAF-based Measurement and Correction Methodology

Focal field contains significant information of antenna deformation, including pointing deviation, main reflector deformation, and subreflector offset. Some focal field analysis methods can be applied to figure out the deformation, e.g., the feed lateral defocusing theory (Zhan et al. 2010) can be used to calculate an antenna's pointing deviation by extracting the position of the maximum focal field amplitude on the focal plane. However, this method fails when the antenna reflector is distorted. Besides, as for Cassegrain reflector antennas, their subreflector offset will also influence the position of the maximum focal field amplitude. As a result, it is impossible to identify the pointing deviation, main reflector deformation, and subreflector offset individually based on the feed lateral defocusing theory. An effective solution is calculating the phase across the antenna aperture and doing a least squares fit for the parameters of antenna deformation according to Butler (Butler 2003). Then, the way of obtaining the antenna aperture field through focal field analysis needs to be studied. Padman (1995) and Rudge (1969) have derived out the relationship between the focal field and aperture field of parabolic reflector antennas by Physical Optics (PO) and scalar diffraction theory. For electrically large antennas, the Geometrical Optics (GO; Holt 1967; Smith & Stutzman 1989), a model of optics that in terms of rays describes light propagation, can also be used to analyze the focal field. In this paper, we are trying to start from the theory of microwave holography, and utilize GO to deduce

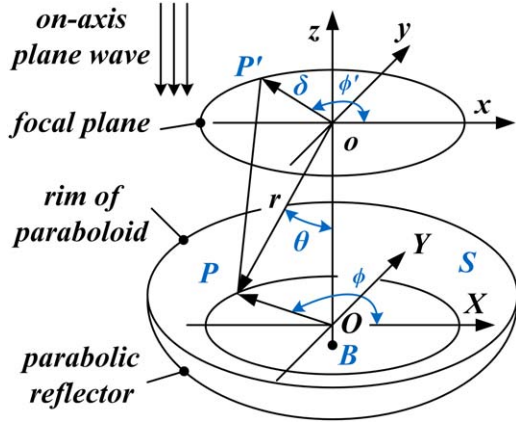


Figure 2. Parabolic reflector antenna and Its focal plane coordinate system; B is the vertex of the paraboloid; P is an arbitrary point on the surface S ; Line PO is perpendicular to the reflector axis and the point O is on the axis; The paraboloid focus (o) is set as the origin of the coordinate system; The reflector axis is chosen as the z -axis; A randomly chosen line on the focal plane going through o is set as the x -axis; The spatial rectangular coordinate system (o - xyz) is established base on the right-handed screw rule; The X -axis of a local coordinate system (O - XYZ) with its origin at point O is parallel to x -axis; A single feed horn is located at point P' with an offset distance δ (oP') from the focal point; The distance between P and the focus is r (oP).

a new main reflector deformation measurement method based on PAF, that is PAF holography.

2.1. Theoretical Derivation of PAF Holography

A parabolic reflector antenna and its focal plane coordinate system are shown in Figure 2. In the theory of microwave holography, a parabolic reflector antenna's far-field pattern is the integration of a function consisting of the induced current distributed around the parabolic surface, the wavenumber, the focal length, the paraboloid correction factor, and the reflector surface deformation distribution (Rochblatt & Seidel 1992; Rochblatt et al. 1995). According to the reciprocity principle, it is known that as for far-field single-carrier or narrowband on-axis incident signals, the receiving signal of a feed element (single feed horn in microwave holography) placed on the focus can be written as (Rochblatt & Seidel 1992)

$$T(0, 0) = \iint_S |J(x, y)| e^{-j2kF + j\frac{4\pi\epsilon(x,y)}{\lambda} \cos \xi} dx dy, \quad (1)$$

where $T(0, 0)$ is the receiving signal at the focus $o(0, 0)$; $J(x, y)$ designates the induced current distributed around the parabolic surface S ; k stands for the wavenumber, i.e., $2\pi/\lambda$; λ is the wavelength; F is the focal length (or equivalent focal length of a Cassegrain reflector antenna); $\epsilon(x, y)$ is the reflector surface deformation distribution; $\cos \xi$ is the paraboloid correction factor, i.e., $1/\sqrt{1 + (x^2 + y^2)/(4F^2)}$. It should be noted that the above and following equations in PAF holography are similar for Cassegrain reflector antennas by using the concept

of equivalent paraboloid (Rahmat-Samii 1984), i.e., replacing the focal length by the equivalent focal length, only like the equations for Cassegrain reflector antennas in microwave holography.

If the feed element is not necessarily placed on the focus, in other words, it is placed on an arbitrary point P' on the focal plane, the receiving signal will be slightly different (Laviada Martinez et al. 2014). It is modified by adding an item to the integrand and can be expressed as

$$T(\Delta x, \Delta y) = \iint_S |J(x, y)| e^{-j2kF + j\frac{4\pi\epsilon}{\lambda} \cos \xi} e^{-jk\Delta r} dx dy, \quad (2)$$

where $(\Delta x, \Delta y)$ is the x and y coordinate value of the arbitrary point P' on the focal plane; Δr is the optical path difference, i.e., $|PP'| - |PO|$ in Figure 2.

The optical path difference Δr in Equation (2) can be calculated as

$$\begin{aligned} \Delta r &= \sqrt{r^2 + \delta^2 - 2r\delta \cos \theta_{r\delta}} - r \\ &= r\sqrt{1 + \frac{\delta^2}{r^2} - 2\frac{\delta}{r} \cos \theta_{r\delta}} - r, \end{aligned} \quad (3)$$

where $\theta_{r\delta}$ is the angle $\angle PoP'$ in Figure 2. Since $\frac{\delta^2}{r^2} - 2\frac{\delta}{r} \cos \theta_{r\delta}$ is very small, we can use Taylor's expansion method for the square root, then Equation (3) can be approximated as

$$\Delta r \approx -\delta \sin \theta \cos(\phi - \phi'). \quad (4)$$

Equation (4) is under the condition that $\delta/r \ll 1$ and ignoring orders higher than $(\delta/r)^2$. By expanding $\cos(\phi - \phi')$ in Equation (4) and considering that $\delta \cos \phi' = \Delta x$, $\delta \sin \phi' = \Delta y$, we can obtain

$$\Delta r = -(\Delta x \cos \phi + \Delta y \sin \phi) \sin \theta. \quad (5)$$

Substituting Equation (5) into (2), then the receiving signal of any feed element placed on the focal plane can be approximately written as

$$\begin{aligned} T(\Delta x, \Delta y) &= \iint_S |J(x, y)| e^{-j2kF + j\frac{4\pi\epsilon}{\lambda} \cos \xi} e^{jk(\Delta x \cos \phi + \Delta y \sin \phi) \sin \theta} dx dy. \end{aligned} \quad (6)$$

Let $l_F = \sin \theta \cos \phi = \frac{4Fx}{x^2 + y^2 + 4F^2}$, $m_F = \sin \theta \sin \phi = \frac{4Fy}{x^2 + y^2 + 4F^2}$, $u = \frac{\Delta x}{\lambda}$, and $v = \frac{\Delta y}{\lambda}$, then Equation (6) can be written as

$$T(u, v) = \iint_{\Omega} [\tilde{J}(l_F, m_F)] e^{-j2kF + j\frac{4\pi\epsilon}{\lambda} \cos \xi} e^{j2\pi(ul_F + vm_F)} dl_F dm_F. \quad (7)$$

After Fourier transform of $T(u, v)$, we will obtain

$$Q(l_F, m_F) = \mathcal{F}[T(u, v)], \quad (8)$$

where $\mathcal{F}[\dots]$ designates the two-dimensional Fourier transform operator. Then by substituting $l_F = \sin \theta \cos \phi = \frac{4Fx}{x^2 + y^2 + 4F^2}$

and $m_F = \sin \theta \sin \phi = \frac{4Fy}{x^2 + y^2 + 4F^2}$ into Equation (8), we obtain

$$\tilde{Q}(x, y) = Q\left(\frac{4Fx}{x^2 + y^2 + 4F^2}, \frac{4Fy}{x^2 + y^2 + 4F^2}\right). \quad (9)$$

Then, the phase distribution $\Phi(x, y)$ across the antenna aperture is

$$\Phi(x, y) = \text{Phase}\{\tilde{A}(x, y)\} = \text{Phase}\{e^{j2kF}\tilde{Q}(x, y)\}, \quad (10)$$

where $\text{Phase}\{\dots\}$ is the symbol of phase calculation; $\tilde{A}(x, y)$ is the aperture field. Combining Equations (7), (8), (9), and (10), we can find out that reflector surface deformation $\epsilon(x, y)$ of a parabolic reflector antenna can be calculated by

$$\epsilon(x, y) = \frac{\lambda}{4\pi} \sqrt{1 + \frac{x^2 + y^2}{4F^2}} \Phi(x, y). \quad (11)$$

Equation (11) works when there is no other deformation from antenna's pitch and azimuth drive mechanism, subreflector, etc.

The PAF holography equations from (1) to (11) work for both single reflector antennas and Cassegrain reflector antennas according to the concept of equivalent paraboloid. As mentioned above, for Cassegrain reflector antennas, the focal length F in the above equations should be replaced by the equivalent focal length, which is the product of the focal length and the Cassegrain antenna magnification.

2.2. Identification of Pointing Deviation and Subreflector Offset

In Equation (11) of PAF holography, it is provided that there is no other deformation from antenna's pitch and azimuth drive mechanism, subreflector, etc. However, in reality, there is inevitably some deformation from these antenna structures; and it often causes the other two important antenna structure parameters, i.e., pointing deviation and subreflector offset, being not negligible. Considerable pointing deviation and subreflector offset can distinctly change the focal field, as well as the phase distribution across the antenna aperture. The solution is to identify the amount of pointing deviation and subreflector offset by generating a best-fit phase distribution across the aperture (Butler 2003). Then, the residual aperture phase distribution can be used for calculating the main reflector deformation.

The identification of pointing deviation and subreflector offset is also based on the focal field data. Equations (8), (9), and (10) have deduced the phase distribution across the antenna aperture. In reality, it is affected by pointing deviation, subreflector offset, and main reflector deformation, and can be expressed as

$$\Phi(x, y) = \Phi_p(x, y) + \Phi_s(x, y) + \Phi_m(x, y), \quad (12)$$

where $\Phi_p(x, y)$, $\Phi_s(x, y)$, and $\Phi_m(x, y)$ are the aperture phase distribution affected by pointing deviation, subreflector offset, and main reflector deformation respectively. Next, the

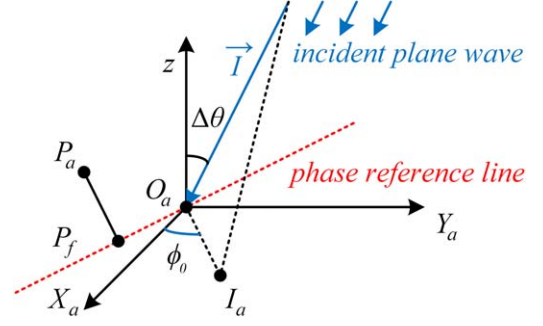


Figure 3. The aperture plane and off-axis incident plane wave.

influence of pointing deviation on the phase distribution across the antenna aperture $\Phi_p(x, y)$ is deduced.

Figure 3 shows that the direction unit vector of the incident plane wave $\mathbf{I}(\Delta l, \Delta m, \Delta n)$ is slightly off-axis by a deviation of $\Delta\theta$. $\Delta\theta = \arcsin\sqrt{(\Delta l)^2 + (\Delta m)^2}$. The angle between the x -axis and the projection ($\overrightarrow{O_a I_a}$) of \mathbf{I} on the aperture plane is ϕ_0 . The red dashed line passing through the coordinate origin O_a on the aperture plane is perpendicular to \mathbf{I} and called as phase reference line. The phase of the aperture field at any points on the phase reference line are equal and set as zero. As for an arbitrary point P_a on the aperture plane, we can draw a line $P_a P_f$ perpendicular to the phase reference line. P_f is the foot point.

Simply like the time difference calculation in radio interferometry (Rogstad et al. 2003), the time difference between the incident plane wave arriving at P_a and P_f is τ , which can simply be calculated as

$$\tau = \overrightarrow{P_f P_a} \cdot \mathbf{I} / c = -\sin \Delta\theta (y \sin \phi_0 + x \cos \phi_0) / c, \quad (13)$$

where c is the speed of light; (x, y) is the x and y coordinate value of the arbitrary point P_a .

Considering that $\sin \Delta\theta \cos \phi_0 = -\Delta l$, $\sin \Delta\theta \sin \phi_0 = -\Delta m$, we can obtain

$$\tau = (y\Delta m + x\Delta l) / c. \quad (14)$$

Then, the phase distribution across the antenna aperture can be expressed as

$$\begin{aligned} \Phi_p(x, y) &= 2\pi f \tau = kx\Delta l + ky\Delta m \\ &= A_{p1}(x, y)\Delta l + A_{p2}(x, y)\Delta m, \end{aligned} \quad (15)$$

where f is the working frequency, i.e., c/λ ; $A_{p1}(x, y) = kx$; $A_{p2}(x, y) = ky$.

The subreflector offset consists of subreflector lateral displacement, axial displacement, and rotation. The influence of subreflector offset on the phase distribution across the

antenna aperture $\Phi_s(x, y)$ has already given by Butler (2003):

$$\begin{aligned} \Phi_s(x, y) = & A_{s1}(x, y)\Delta x_s + A_{s2}(x, y)\Delta y_s + A_{s3}(x, y)\Delta z_s \\ & + A_{s4}(x, y)\Delta\alpha_x + A_{s5}(x, y)\Delta\alpha_y, \end{aligned} \quad (16)$$

where

$$\begin{aligned} A_{s1}(x, y) &= -k \cos \phi_a (\sin \theta_p - \sin \theta_f); \\ A_{s2}(x, y) &= -k \sin \phi_a (\sin \theta_p - \sin \theta_f); \\ A_{s3}(x, y) &= k (\cos \theta_p + \cos \theta_f - 2); \\ A_{s4}(x, y) &= k \sin \phi_a (C - A) (\sin \theta_p + M \sin \theta_f); \\ A_{s5}(x, y) &= -k \cos \phi_a (C - A) (\sin \theta_p + M \sin \theta_f); \end{aligned}$$

θ_p is the angle between the optical axis and a ray from the feed to the subreflector;

$$\sin \theta_p = \frac{r_a/F}{1 + [r_a/(2F)]^2};$$

θ_f is the angle between the optical axis and a ray from the subreflector to the main reflector;

$$\sin \theta_f = \frac{r_a/(MF)}{1 + [r_a/(2MF)]^2};$$

$$\phi_a = \arctan(y/x)$$

$$r_a = \sqrt{x^2 + y^2}$$

$C - A$ is the distance from the primary focus to the subreflector surface along the optical axis;

M is the antenna magnification;

$(\Delta x_s, \Delta y_s)$ is the subreflector lateral displacement;

Δz_s is the subreflector axial displacement;

$\Delta\alpha_x, \Delta\alpha_y$ is the subreflector rotation/tilt around the vertex.

For more details about Equation (16), please refer to Butler (2003). So far, we are able to eliminate or reduce the effects of pointing deviation and subreflector offset by calculating the phase across the antenna aperture and doing a least squares fit for the parameters of the antenna deformation. The residual vector is expressed as

$$\mathbf{R} = \mathbf{B} - \mathbf{A}\mathbf{X} \quad (17)$$

where

$$\mathbf{R} = \{\Phi_m(x_i, y_i)\}_{i=1}^n;$$

$$\mathbf{B} = \{\Phi(x_i, y_i)\}_{i=1}^n;$$

$$\mathbf{A} = \begin{bmatrix} A_{p1}(x_1, y_1) & A_{p2}(x_1, y_1) & A_{s1}(x_1, y_1) & A_{s2}(x_1, y_1) & \cdots & A_{s5}(x_1, y_1) \\ A_{p1}(x_2, y_2) & A_{p2}(x_2, y_2) & A_{s1}(x_2, y_2) & A_{s2}(x_2, y_2) & \cdots & A_{s5}(x_2, y_2) \\ \vdots & \vdots & \vdots & \vdots & \ddots & \vdots \\ A_{p1}(x_n, y_n) & A_{p2}(x_n, y_n) & A_{s1}(x_n, y_n) & A_{s2}(x_n, y_n) & \cdots & A_{s5}(x_n, y_n) \end{bmatrix};$$

$\mathbf{X} = [\Delta l, \Delta m, \Delta x_s, \Delta y_s, \Delta z_s, \Delta\alpha_x, \Delta\alpha_y]^T$ is the vector of antenna deformation parameters.

The least squares fit is done by determining the value of $\Delta l, \Delta m, \Delta x_s, \Delta y_s, \Delta z_s, \Delta\alpha_x, \Delta\alpha_y$ to make $\sum_{i=1}^n \Phi_m^2(x_i, y_i)$ be its minimum. After the least squares fit, the residual phase distribution can substitute the term $\Phi(x, y)$ in Equation (11) to calculate the reflector surface deformation.

2.3. Measurement and Correction System

Here, we propose a deformation measurement and correction system for Cassegrain reflector antennas based on PAF holography, shown in Figure 4. As for a single reflector antenna, its deformation measurement and correction system based on PAF holography is similar except that the subreflector system is absent. Focal field analysis is the core and fundamental part in the system. Mathematically, the focal field analysis part is done by calculating the equations we have derived in Sections 2.1 and 2.2. The system contains two main procedures, that is the measurement procedure (denoted in light blue) and the correction procedure. The latter is done by mechanical adjustment (denoted in light olive) and electrical compensation (denoted in light red).

(1) The measurement procedure

The incident plane wave is reflected and converged by the reflector to reach the focal plane. Each feed element of the PAF receives a portion of the incident energy. After being processed by the low noise amplifier (LNA), down converter (DC), and A/D converter, the receiving signal of each feed element will be sent to the Field Programmable Gate Array (FPGA). In FPGA, the focal field is recovered first using cubic spline interpolation based on the receiving signals. Then, by analyzing the amplitude and phase distribution of the focal field, i.e., calculating the equations we have derived in Sections 2.1 and 2.2, all the parameters of antenna deformation including main reflector deformation ϵ , pointing deviation ($\Delta l, \Delta m$), and subreflector offset ($\Delta x_s, \Delta y_s, \Delta z_s, \Delta\alpha_x, \Delta\alpha_y$) will be obtained.

(2) The correction procedure

After focal field analysis, the pointing deviation ($\Delta l, \Delta m$), main reflector deformation ϵ , and subreflector offset information ($\Delta x_s, \Delta y_s, \Delta z_s, \Delta\alpha_x, \Delta\alpha_y$) will be obtained and be fed back to the pitch and azimuth drive system, main reflector surface control system, and subreflector control system to correct large or slowly changing deformations. For instance, based on the feedback received, the pitch and azimuth drive system can eliminate the pointing deviation by setting an adjustment quantity of $(-\Delta l, -\Delta m)$ to the antenna pointing direction. The mechanical adjustment procedure of main reflector deformation using actuators mounted on the antenna framework is illustrated in Wang et al. (2017). According to the subreflector offset information received, the subreflector control system can rotate and move the subreflector to its optimum posture and position. Next, weighted complex coefficients are generated for each feed element based on Conjugate Field Matching (CFM) (Cherrette et al. 1989) method. After signal synthesis, the residual or rapidly changing deformation will be electrically compensated. Multiple FPGAs will synthesize multi-beam data, and the data will be transmitted to the GPU for further processing according to the antenna's actual observation needs.

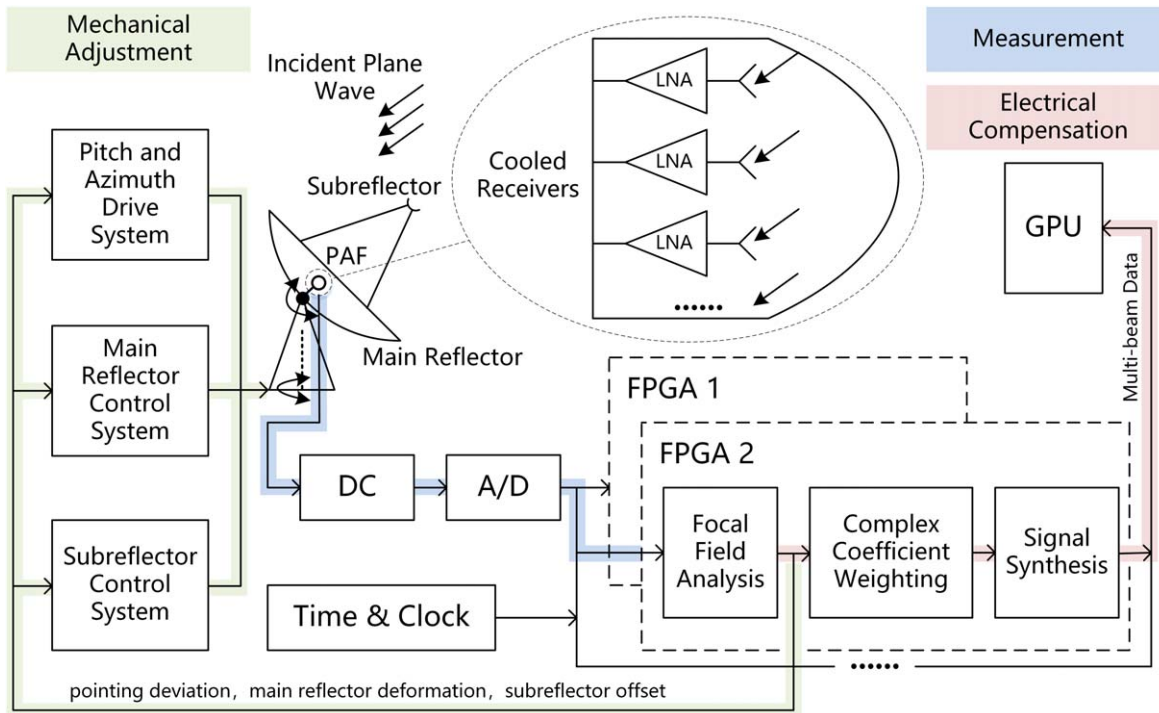


Figure 4. Measurement and correction system based on PAF holography.

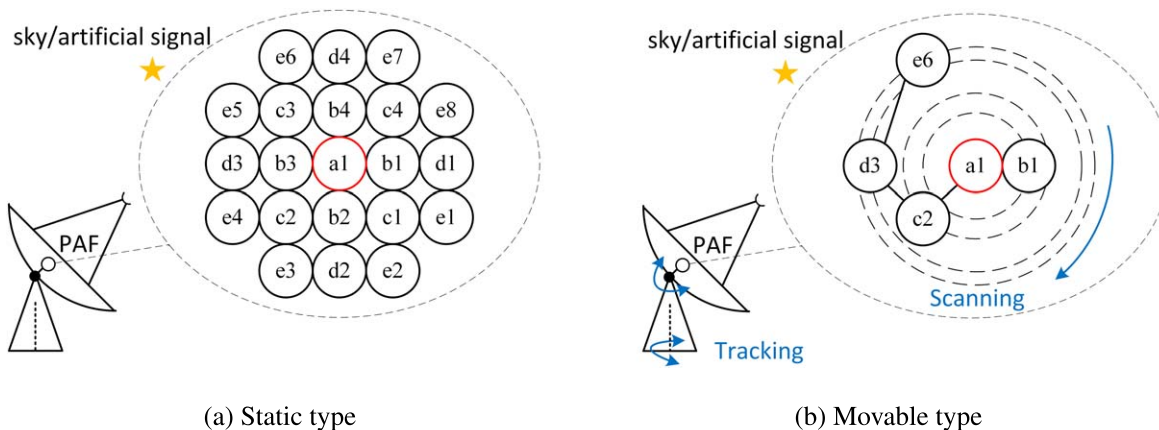


Figure 5. Two kinds of measurement methods for focal field acquisition.

Before focal field analysis, in the measurement procedure, there are two primary measurement methods to obtain the focal field of a Cassegrain reflector antenna by using two kinds of focal plane arrays, shown in Figure 5. The two measurement methods are also feasible for obtaining the focal field of a single reflector antenna.

(1) The static-type focal plane array

As it shows in Figure 5(a), by setting the antenna pointing toward a known sky/artificial signal, such as a geostationary satellite, a radio source, or an artificial beacon, the static-type

focal plane array can get the focal field data instantaneously. It is a real-time measurement in this case. It should be noted that, the element spacing in Figure 5(a) must meet the requirements of sampling theorem, so that one can calculate out the focal field immediately based on the receiving signals obtained by each feed element. Every single receiving signal of feed elements should do a cross-correlation operation with the receiving signal of center feed element, the red one in Figure 5(a), to reduce the influence of noise, especially when the sky/artificial signal is weak.

(2) The movable-type focal plane array

The focal field acquisition process in Figure 5(b) is slightly time-consuming due to a fact that we have to spend some time on scanning the focal plane and tracking the radio source at the same time. Nonetheless, compared with far-field microwave holography, the time spent on scanning the focal plane is much less. If the feed elements are arranged at positions exactly like Figure 5(b) and their supports are rigid connected, then a quick scanning motion of feed elements, i.e., a full rotation of the supports around center feed element, the red one in Figure 5(b), will drive the feed elements a1, b1, c2, d3, and e6 to accomplish focal plane scanning. It should be noted that in Figure 5(b), the position of the feed elements on the element support should be adjustable so that astronomical engineers can change the position, as well as the size of the feed elements, according to their actual observation needs. If the sky/artificial signal is a geostationary satellite or a static artificial beacon, then the tracking motion is not needed due to the relatively stationary state of the antenna. Similarly, every single receiving signal of feed elements in Figure 5(b) should also do a cross-correlation operation with the receiving signal of center feed element to reduce the influence of noise, especially when the sky/artificial signal is weak.

Generally, the number of feed elements in static-type focal plane array is far more than in movable-type focal plane array. The static-type focal plane array has the advantage of obtaining the focal field data instantaneously while the movable-type focal plane array has inevitably take some time to do mechanical scanning. One way to reduce the scanning time is using more feed elements. For example, we can add feed elements b3, c4, d1, and e2 on the opposite side of b1, c2, d3, and e6 respectively in Figure 5(b). As a result, a half rotation of the supports around the center feed element will drive the feed elements to accomplish focal plane scanning, which means the scanning time can be cut down by half. Of course, we can continue adding more feed elements, but more feed elements will then bring up the problem of mutual coupling, especially when the element spacing is small.

By appropriately designing the positions of each scanning feed element making them scattered individually, the mutual coupling effect of a movable-type focal plane array with relatively few feed elements can be reduced. When the element spacing of a static-type focal plane array is very small, one should consider changing to use a movable-type focal plane array to reduce mutual coupling effect. If a movable-type focal plane array has only one feed element, then there will be no more mutual coupling effect. But at the same time, the scanning time will increase much because the only feed element has to do both radial and circular movements to accomplish focal plane scanning. In summary, compared with far-field microwave holography, in which the whole antenna has to do radio source scanning motions (Wang et al. 2019), the measurement time of PAF holography can be much shorter either using the

movable-type focal plane array or the static-type focal plane array in Figure 5.

3. Numerical Simulation and Error Analysis

3.1. Numerical Simulation

To verify the proposed theory of PAF holography, a program based on the theory is developed in MATLAB; and the verification process is as follows:

- (1) Import an antenna's reflector surface profile obtained by traditional measurement methods (e.g., laser scanning) or using empirical equations (Rahmat-Samii 1990) into an electromagnetic simulation software (e.g., GRASP). The antenna's focal field is simulated by the excitation of an incident planar electromagnetic wave, whose propagation direction is exactly opposite to the antenna's current pointing direction.
- (2) Export the antenna's focal field data obtained in the last step and import it into MATLAB. Apply the PAF holography program, then the main reflector's surface error cloud map is obtained.
- (3) Compare the main reflector's surface error cloud maps obtained by traditional measurement methods and PAF holography. The more consistent the display of surface error cloud maps, the higher accuracy of PAF holography is.

The structure model of WRT is developed in GRASP. There is no pointing deviation or subreflector offset in the model. Two surface profiles of the main reflector are generated using both the laser scanning data we have obtained in actual measurement (Fu et al. 2022) and empirical equations referred to Rahmat-Samii (1990). In this paper, we use SPLS to denote the main reflector surface profile obtained by laser scanning when WRT is at the elevation angle of 90° under Sun irradiation and take SPEE to denote the main reflector surface profile generated by the following empirical equations (Rahmat-Samii 1990)

$$\begin{cases} z_P = \frac{x_P^2 + y_P^2}{4F_{\text{WRT}}} + \epsilon_B \\ \epsilon_B = 0.005 \left(\frac{2r_P}{D_{\text{WRT}}} \right)^3 \cos(2\phi_P) \end{cases}, \quad (18)$$

where (x_P, y_P, z_P) is the main reflector profile; F_{WRT} is the focal length; ϵ_B is the slowly varying main reflector deformation; D_{WRT} is the main reflector diameter; r_P, ϕ_P are the polar radius and polar angle respectively of any point on the main reflector surface. Primary parameters of the Wuqing 70 m Radio Telescope are shown in Table 2.

Figure 6 shows the amplitude and phase distribution of the antenna focal field obtained in GRASP under the influence of SPLS and SPEE, respectively. By applying the PAF

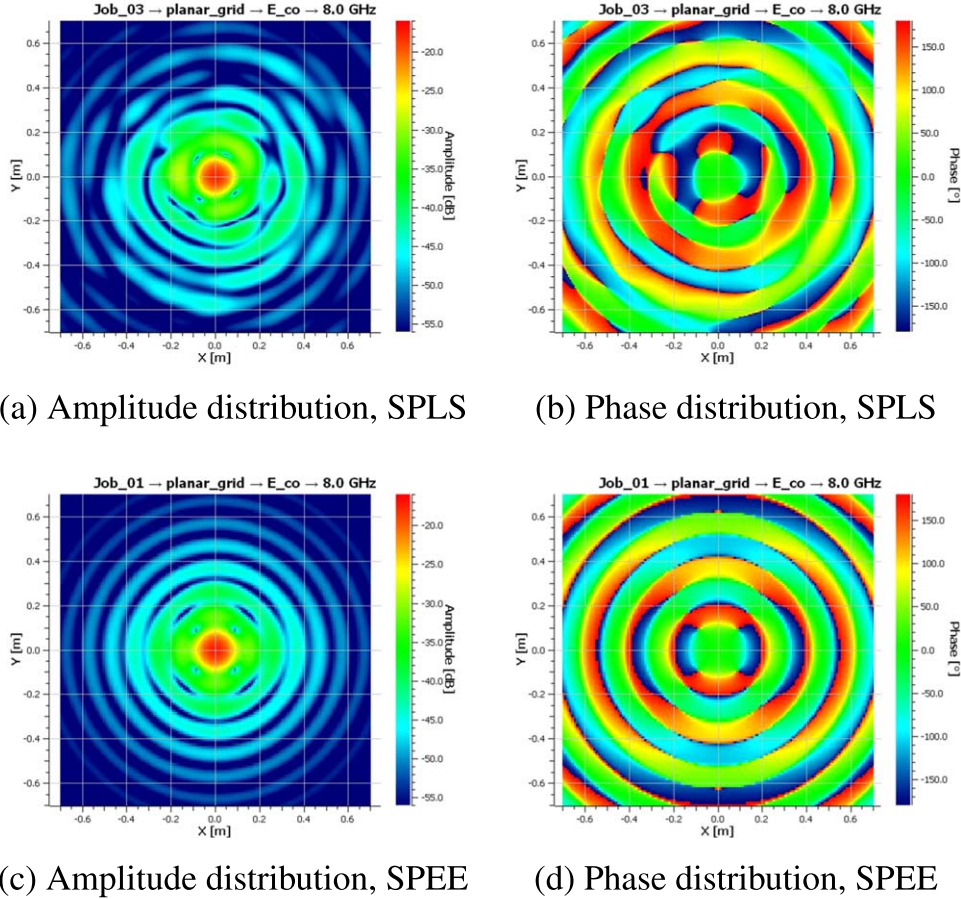


Figure 6. Simulated focal field of the WRT with distorted reflector SPLS and SPEE.

holography program we developed in MATLAB, the surface error cloud maps of WRT are obtained and shown in Figure 7. The far-field patterns of WRT under the influence of SPLS and SPEE are also simulated. Then, by applying the far-field microwave holography equations (Rochblatt & Seidel 1992), the other two surface error cloud maps based on microwave holography are also obtained and displayed in Figure 7. To reduce the simulation time, the working frequency is set as 8 GHz. There are 129×129 sampling points in the sampling range of $1.4 \text{ m} \times 1.4 \text{ m}$ in PAF holography, which means the sampling interval is about 0.011 m, i.e., 0.29 times of the wavelength. In the far-field microwave holography, the number of sampling points is also 129×129 , and the sampling range is $0.016 \text{ rad} \times 0.016 \text{ rad}$.

Figures 7(a), (b), and (c) depict the surface error cloud maps of WRT with distorted reflector SPLS obtained by laser scanning, microwave holography, and PAF holography, respectively. The corresponding calculated rms errors of reflector deformation are 1.351, 1.716, and 1.268 mm. The outer part, especially the right side, lower right corner, left side, and upper right corner of these three surface error cloud maps

Table 2
Parameters of the WRT (Kong et al. 2022)

Parameter	Value
Main reflector diameter	70,000 mm
Subreflector diameter	6600 mm
Distance between foci	16547.8 mm
Eccentricity	1.26
Magnification	8.6923
Equivalent f/d ratio	2.6077
Equivalent focal length	182,539 mm
Half-angle subtended by subreflector at the feed	$10^\circ 8'$

all shows good consistency. The inner part of these three surface error cloud maps also shows good consistency except the upper right section where steep-varying deformation occurs. Actually, the steep-varying deformation occurring at the upper right of the reflector's inner part is because of occlusion during laser scanning, seen from Fu et al. (2022). As we can see, both microwave holography and PAF holography are not good at measuring steep-varying deformation. The

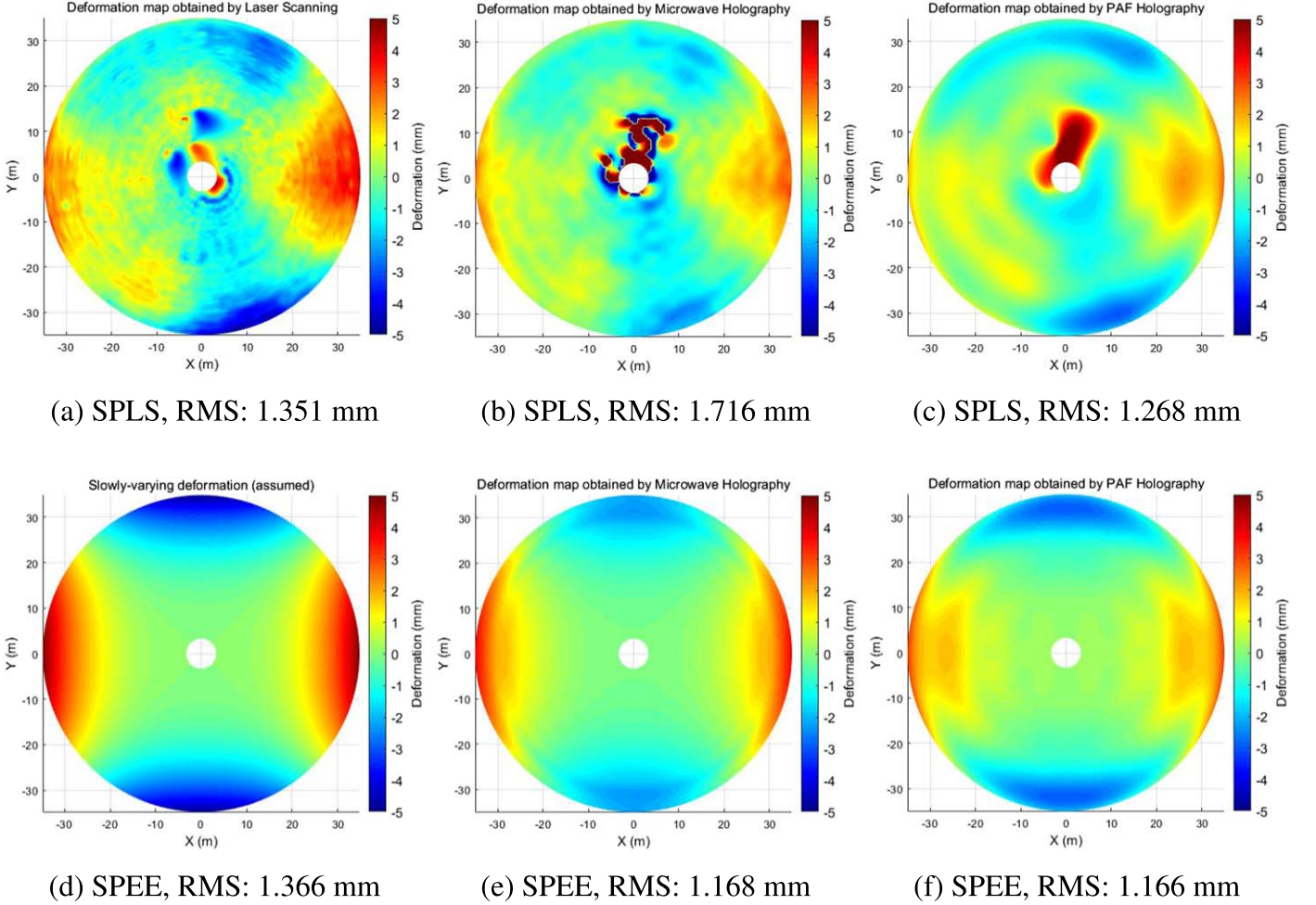


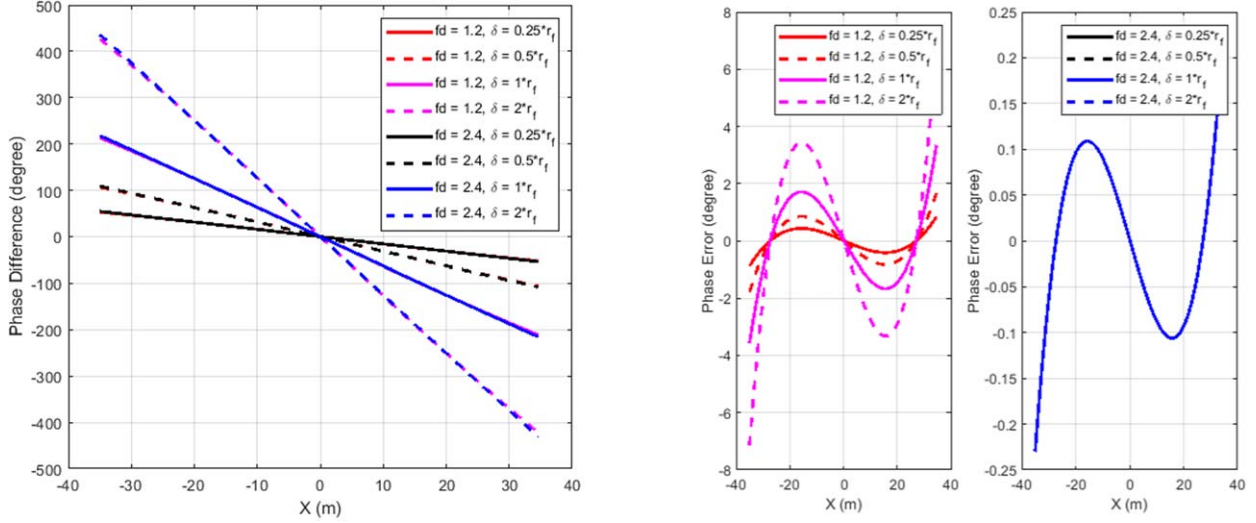
Figure 7. Surface error cloud maps obtained by different measurement methods.

reason is that it can bring multiple reflections at local areas where steep-varying deformation occurs. As a result, the amplitude distribution of the antenna's far-field will be heavily scattered. So will be the amplitude distribution of the focal field, as it shows in Figure 6(a). There is a clear difference between Figures 6(a) and (c). The latter is simulated in the condition that the deformation is slowly varying all over the distorted reflector. Figures 7(d), (e), and (f) are surface error cloud maps of WRT with distorted reflector SPEE obtained by empirical equations in Equation (18), microwave holography, and PAF holography, respectively. The corresponding calculated rms errors of reflector deformation are 1.366 mm, 1.168 mm, and 1.166 mm. These three surface error cloud maps show good consistency, which indicates that the theory of PAF holography is feasible. There is an rms gap between Figures 7(f) and (d). It is due to the fact that the sampling range of focal field, i.e., the space domain of 2D Fourier transform, is limited, not the whole focal field, in our

simulation based on PAF holography. Similar rms gap occurs when comparing Figures 7(e) and (d). The reason is similar. In microwave holography, the sampling range of far-field is also limited, not the whole far-field.

3.2. Error Analysis

The measurement result of PAF holography inevitably has some error due to the approximation of Equation (4) in Section 2.1. The corresponding phase error can be simulated. Here, we set a parabolic reflector antenna with aperture diameter of 70 m. Its working frequency f_w is set as 26 GHz. Considering that the reflector surface is circularly symmetric, we can simply look into the one-dimensional situation. The approximation of Equation (4) can be done through a linearity fitting by the method of least squares. Let the approximated path difference by linear fitting be Δr_a , then the corresponding


 (a) Real phase difference ΔP_r

 (b) Phase truncation error ΔP_{ra-r} by linear fitting

Figure 8. Real phase difference and phase truncation error.

phase truncation error ΔP_{ra-r} can be calculated as

$$\Delta P_{ra-r} = 2\pi f_w \frac{\Delta r_a - \Delta r}{c} \quad (19)$$

The phase truncation error ΔP_{ra-r} and the corresponding real phase difference ΔP_r , i.e., dividing the optical path difference Δr in Equation (3) by $c/(2\pi f_w)$, are calculated and depicted in Figure 8. The two simulation variables are the ratio of the focal length (or equivalent focal length) to aperture diameter (f/d in the legend), and the distance (δ in the legend) between the feed element and the focus (or secondary focus) of the antenna. r_f designates the radius of the first dark ring of the focal field of an undistorted reflector antenna, and it can be calculated by Yang (1993)

$$r_f = 0.6099 \frac{\lambda}{\theta_0}, \quad (20)$$

where θ_0 is the half-angle subtended by subreflector at the feed for a Cassegrain reflector antenna or the half-angle subtended by aperture at the feed for a single reflector antenna. θ_0 and the ratio of the focal length (or equivalent focal length) to aperture diameter (f/d) are negatively correlated, thus r_f and f/d ratio are positively correlated.

The phase difference curves in Figure 8(a) imply that for reflector antennas with a large f/d ratio, the real phase difference is almost a straight line. Comparing the phase truncation errors when the f/d ratio is 1.2 and 2.4 in Figure 8(b), we can conclude that for either Cassegrain reflector antennas or single reflector antennas with the larger f/d ratio, the approximation of Equation (4) in Section 2.1 is more reasonable. Besides, it should be noted that when the feed

element is too far away from the focus, i.e., δ is too large, as the magenta and dashed curve ($f/d = 1.2, \delta = 2r_f$) shown in Figure 8(b), the phase truncation error will be significant so that the approximation is no more accurate. The interesting thing is that if we double the f/d ratio, then the distance between the feed element and the focus seems to have very little influence on the phase truncation error, as the overlapping curves shown in Figure 8(b). As for single reflector antennas, PAF holography has to be conducted with smaller PAF due to their smaller f/d ratio. Fortunately, single reflector antenna's focal field energy is more concentrated compared with Cassegrain reflector antennas according to Yang (1993). Therefore, using a small PAF to do PAF holography for single reflector antennas is also feasible. Additionally, it should be noted that if the deformation of a single or Cassegrain reflector antenna is very large, its focal field energy will be scattered severely, resulting in inaccurate measurement result at regions close to the edge of the reflector. Thus, the PAF holography result needs to be corrected according to the actual situation.

4. Conclusion and Prospect

This paper derived the theory of PAF holography and established a new deformation measurement and correction system for large reflector antenna based on PAF holography. It can be used to measure and correct the deformation of the main reflector surface for both single reflector antennas and Cassegrain antennas, and by using the static-type PAF to measure deformation, the real-time measurement of surface accuracy, and real-time correction of deformation caused by wind load, Sun irradiation, or antenna gravity, can be achieved.

The proposed measurement methodology is verified by numerical simulation, and its measurement error is analyzed. The simulation results show good consistency between the proposed PAF holography method and traditional measurement methods, which indicates that the theory of PAF holography is feasible.

The correction, i.e., electrical compensation, of main reflector deformation can easily be done by applying the commonly used Conjugate Field Matching (CFM) method. The key is determining the appropriate array layout, number of feed elements, and element spacing. The performance of PAFs with different numbers of elements and element spacing is investigated in a separate paper which will be published later. In the following research, a small size PAF will be designed, manufactured, tested, and optimized. In order to do the experiment, other systems of the WRT, such as the antenna receiving system and data process terminal used for PAF, are also needed to be developed. After optimization, we will deploy the small size PAF on the secondary focal feed of WRT, and then conduct some PAF holography and electrical compensation experiments to further verify the proposed measurement and correction methodology.

Acknowledgments

This work was funded by the Astronomical Joint Fund of the National Natural Science Foundation of China and Chinese Academy of Sciences under Nos. 12373103, 12073048 and 62227901.

ORCID iDs

Yu-Chen Liu  <https://orcid.org/0000-0001-6831-4370>

References

- Amitay, N., & Zucker, H. 1972, *ITAP*, **20**, 49
- Balanis, C. A. 2005, *Antenna Theory Analysis and Design* (3rd ed.; New York: Wiley)
- Beresford, R., Cheng, W., Hampson, G., et al. 2017, in 2017 XXXIIInd General Assembly and Scientific Symp. Int. Union of Radio Science (URSI GASS) (Montreal, QC: IEEE), 1
- Blank, S. J., & Imbriale, W. A. 1988, *ITAP*, **36**, 1351
- Burnett, M. C., Kunzler, J., Nygaard, E., et al. 2020, in 2020 XXXIIIrd General Assembly and Scientific Symp. Int. Union of Radio Science (Rome: IEEE), 1
- Butler, B. J. 2003, Requirements for Subreflector and Feed Positioning for ALMA Antennas, ALMA Memo. 479, NRAO, <http://alma.nrao.edu/memos/html-memos/alma479/memo479.pdf>
- Carretti, E., Aresu, G., Bachetti, M., et al. 2017, in 2017 Int. Conf. on Electromagnetics in Advanced Applications (ICEAA) (Verona, Italy: IEEE), 1739
- Cherrette, A. R., Acosta, R. J., Lam, P. T., & Lee, S.-W. 1989, *ITAP*, **37**, 966
- Chippendale, A. P., Beresford, R. J., Deng, X., et al. 2016, in 2016 Int. Conf. on Electromagnetics in Advanced Applications (ICEAA) (Cairns, QLD, Australia: IEEE) **909-912**
- Deng, X., Chippendale, A. P., Hobbs, G., et al. 2017, *PASA*, **34**, e026
- Dong, J., & Liu, Q.-H. 2021, *ScChG*, **51**, 029503
- Fu, L.-B., Liu, J.-J., Yan, W., et al. 2022, *RAA*, **22**, 095001
- Gale, D. M., Leon-huerta, A., Cuevas, L. C., et al. 2016, *Proc. SPIE*, **9912**, 99124F
- Guo, K.-J., Wang, B.-T., & He, X.-G. 2021, *Electro-Mechanical Engineering*, **37**, 41
- Han, Y.-B., & Zhong, L.-Q. 2016, *Int. J. Antennas and Propagation*, **2016**, 5357368
- Holst, C., Nothnagel, A., Blome, M., et al. 2014, *JAGeo*, **9**, 1
- Holst, C., Schunck, D., Nothnagel, A., et al. 2017, *Senso*, **17**, 1833
- Holt, F. S. 1967, Application of Geometrical Optics to the Design and Analysis of Microwave Antennas, Physical Sciences Research Papers AD661561, Office of Aerospace Research, United States Air Force, <https://apps.dtic.mil/sti/pdfs/AD0661561.pdf>
- Hunter, T. R., Schwab, F. R., White, S. D., et al. 2011, *PASP*, **123**, 1087
- Imbriale, W. A., & Hoppe, D. J. 2000, TMOPR 42-140, Jet Propulsion Laboratory (JPL), https://ipnpr.jpl.nasa.gov/progress_report/42-140/140L.pdf
- Kong, D.-Q., Li, C.-L., Zhang, H.-B., et al. 2022, *RAA*, **22**, 035013
- Laviada Martinez, J., Arbolea-Arbolea, A., & Alvarez-Lopez, Y. 2014, *IAWPL*, **13**, 43
- Li, L.-C., Staveley-Smith, L., & Rhee, J. 2021, *RAA*, **21**, 030
- Liu, K., Ye, Q., & Meng, G. 2016, *EIL*, **52**, 12
- Morison, I. 2007, *Astronomy & Geophysics*, **48**, 523
- Navarrini, A., Nesti, R., & Schirru, L. 2019, in 2019 IEEE II Ukraine Conf. Electrical and Computer Engineering (UKRCON) (Lviv, Ukraine: IEEE), 137
- Padman, R. 1995, in Emerson DT and Payne JM. Multi-Feed Systems for Radio Telescopes, ASP Conf. Ser. 75, ed. D. T. Emerson & J. M. Payne (San Francisco, CA: ASP), **3**
- Pei, X., Wang, N., Werthimer, D., et al. 2022, *RAA*, **22**, 045016
- Rahmat-Samii, Y. 1984, *RaSc*, **19**, 1205
- Rahmat-Samii, Y. 1990, *IAPM*, **32**, 20
- Rochblatt, D. J. 1998, in 1998 IEEE Aerospace Conf. Proc. (Snowmass, CO: IEEE) **441-452**
- Rochblatt, D. J., & Seidel, B. L. 1992, *ITMTT*, **40**, 1294
- Rochblatt, D. J., Withington, P. M., & Jackson, H. J. 1995, *TDAPR*, **42-121**, 252
- Rogstad, D.-H., Mileant, A., & Pham, T.-T. 2003, *Antenna Arraying Techniques in the Deep Space Network* (New York: Wiley)
- Roshi, D. A., Shillue, W., Simon, B., et al. 2018, *AJ*, **155**, 202
- Rudge, A. W. 1969, *EIL*, **5**, 510
- Rudge, A. W., & Davies, D. E. N. 1970, *Proc. Instn. Electr. Engineers*, **117**, 351
- Ruze, J. 1966, *Proc. IEEE*, **54**, 633
- Schirru, L., Pisanu, T., Navarrini, A., et al. 2019, in 2019 IEEE II Ukraine Conf. Electrical and Computer Engineering (UKRCON) (Lviv, Ukraine: IEEE), 133
- Serra, G., Bolli, P., Busonera, G., et al. 2012, in *SPIE Astronomical Telescopes + Instrumentation*, ed. Larry M. Stepp, Roberto Gilmozzi, & Helen J. Hall (Amsterdam: SPIE), **84445W**
- Smith, W. T., & Stutzman, W. L. 1989, in *Proc. IEEE Energy and Information Technologies in the Southeast* (Columbia, SC: IEEE), 214
- Tang, L.-L. 2015, Dissertation of Nanjing University of Science and Technology, Nanjing University of Science and Technology in Chinese
- Van Cappellen, W. A., Oosterloo, T. A., Verheijen, M. A. W., et al. 2022, *A&A*, **658**, A146
- Wang, C.-S., Li, J.-J., Zhu, M.-B., et al. 2013, *Electro-Mechanical Engineering*, **29**, 5
- Wang, J.-Q., Zhao, R.-B., Yu, L.-F., et al. 2019, *ScChG*, **49**, 109501
- Wang, J.-Q., Zuo, X.-T., Michael, K., et al. 2017, *ScChG*, **47**, 099502
- Wang, N. 2014, *ScChG*, **44**, 783
- Wang, Z., Kong, D.-Q., Zhang, H.-B., et al. 2022, *RAA*, **22**, 095013
- Wu, Y. 2013, Research on the Phased Array Feed Technology for the Radio Telescopes, Dissertation of Xidian University, Xidian University in Chinese
- Wu, Y., Du, B., Liu, X.-M., et al. 2013, *J. Electron. & Information Technology*, **35**, 1236
- Yang, K.-Z. 1993, *New Technologies for Modern Reflector Antennas* (Beijing: Posts and Telecommunications Press)
- Yu, Y.-Z., Han, L., Zhou, S., et al. 2016, *AR&T*, **13**, 408
- Zhan, D.-Z., Jin, C.-J., Yu, J.-L., et al. 2010, *AR&T*, **7**, 295